Published in final edited form as:
Phys Med Biol. 2005 September 7; 50(17): 4225–4241.

Tomographic bioluminescence imaging by use of a combined optical-PET (OPET) system: a computer simulation feasibility study

George Alexandrakis[1], **Fernando R Rannou**[2], and **Arion F Chatziioannou**[1]
1 *David Geffen School of Medicine at UCLA, Crump Institute for Molecular Imaging, University of California, 700 Westwood Plaza, Los Angeles, CA 90095, USA*

2 *Departamento de Ingenieria Informatica, Universidad de Santiago de Chile (USACH), Av. Ecuador 3659, Santiago, Chile*

Abstract

The feasibility and limits in performing tomographic bioluminescence imaging with a combined optical-PET (OPET) system was explored by simulating its image formation process. A micro-MRI based virtual mouse phantom was assigned appropriate tissue optical properties to each of its segmented internal organs at wavelengths spanning the emission spectrum of the firefly luciferase at 37 °C. The TOAST finite-element code was employed to simulate the diffuse transport of photons emitted from bioluminescence sources in the mouse. OPET measurements were simulated for single-point, two-point and distributed bioluminescence sources located in different organs such as the liver, the kidneys and the gut. An expectation maximization code was employed to recover the intensity and location of these simulated sources. It was found that spectrally resolved measurements were necessary in order to perform tomographic bioluminescence imaging. The true location of emission sources could be recovered if the mouse background optical properties were known *a priori*. Assumption of a homogeneous optical property background proved inadequate for describing photon transport in optically heterogeneous tissues and lead to inaccurate source localization in the reconstructed images. The simulation results pointed out specific methodological challenges that need to be addressed before a practical implementation of OPET-based bioluminescence tomography is achieved.

1. Introduction

The translation of putative cancer therapy agents to the clinic can greatly be facilitated by non-invasive imaging methods that allow high throughput screening in animal models. Additionally, time-lapse whole body imaging of animals bearing xenografts of appropriately labelled cancer cells can provide new information on tumour growth dynamics and metastasis patterns that is not possible to obtain by invasive experimental approaches. Bioluminescence imaging has recently emerged as a modality that can meet these research needs by use of low cost and easy to operate equipment (Contag *et al* 1998). The capacity to detect optical photons with high efficiency and the intrinsically low autoluminescence background of mice make bioluminescence detection a very sensitive technique if photon sources are located near the tissue surface. However, most bioluminescence probes currently in use emit the bulk of their optical signal at green wavelengths and are therefore attenuated very strongly if they are located deep in tissues (Troy *et al* 2004). In addition, planar images of weak sources near the surface

E-mail: ArChatziioann@mednet.ucla.edu.

(1)Author: Please provide journal title in ‘Arridge *et al* 1993’ and ‘Contag *et al* 1998’.

could look identical to ones produced by stronger sources deeper in tissue (Kuo *et al* 2004). Tomographic imaging is therefore required for source localization. The capacity of bioluminescence imaging in producing accurate tomographic reconstructions is a topic of ongoing investigation (Kuo *et al* 2004, Wang *et al* 2004, Chaudhari *et al* 2005).

Positron emission tomography (PET) is a well-established modality for small animal imaging (Tai *et al* 2001, Chatziioannou 2002) and several commercial systems are now available. PET can perform functional imaging of physiological processes with exquisite specificity if an appropriate radiolabeled tracer analogue exists. New PET tracers that allow monitoring of previously inaccessible physiological processes or simply ones that confer increased specificity of detection in small animals can subsequently be tested on humans in the clinic without modification (Ray *et al* 2004). Despite this direct translational advantage PET is hindered by the need to use positron emitting tracers, which usually requires the presence of a nearby cyclotron. This makes PET methodology a valuable but expensive and lower throughput tool.

A single device that will perform simultaneously both optical and PET (OPET) imaging on the same animal is currently under development in our laboratory (Prout *et al* 2004, Rannou *et al* 2004). The OPET radial field of view is only slightly larger than the mouse torso (figure 1). Both bioluminescence and scintillation photons from the converted annihilation gammas are detected by photomultiplier tubes at the back end of the PET crystals and the two signal types are distinguished by their very different pulse amplitudes (Prout *et al* 2004). Use of fusion reporter gene probes co-expressing optical and PET signals under the same promoter (Ray *et al* 2003) will produce images that are intrinsically co-registered in space. This unique advantage of the OPET device will enable direct comparison of how well the optical and PET modalities can localize and how sensitively they can detect emission sources existing at different tissue depths.

The purpose of this work is to explore the feasibility and limits in performing bioluminescence tomographic measurements with the proposed OPET system, by simulating its image formation process. A mouse micro-MRI image volume (Segars *et al* 2004) provided the anatomical features for a virtual phantom. Each of the segmented tissues was assigned appropriate optical properties which were collected from the literature and were adjusted for blood content and oxygenation levels (see the methods). OPET measurements were simulated for single-point, two-point and distributed bioluminescence sources located in different organs such as the liver, the kidneys and the gut. An expectation maximization (EM) code was employed to recover the intensity and location of these simulated sources. The effects of spectrally-resolved measurements, detector spatial sampling and the adequacy of approximating the mouse background optical properties by a uniform medium were explored.

2. Methods

In order to assess the effect of background optical properties on the OPET image formation process, photon propagation calculations were performed in an optically heterogeneous virtual mouse phantom. The anatomical definitions of the different tissues in this phantom were provided by a publicly available time-gated high resolution MRI image volume known as the mouse phantom for molecular imaging research (Segars *et al* 2004) (MOBY). Different time instances of the mouse image volume could be generated by use of a program utilizing the natural spline definitions of its segmented organ volumes (Segars *et al* 2004). For our simulations we used the first time gate of that image volume and we implemented some further alterations in order to simplify computations: only the mouse torso was simulated, from the neck to the base of the tail, the tissue surface was padded out to a perfect cylinder of 27 mm diameter and the image volume was re-sampled to 2 mm size voxels (figure 2). The amount of padding did not exceed 2 mm in the radial direction at any location near the torso surface.

As the original MOBY image did not include the mouse skin, the latter was defined as the first 2 mm (one voxel) in from the cylinder's surface. As a result, the padded volume voxels were defined to be occupied by skin. The MOBY-defined organ volumes for the gall-bladder, vas deferens, and testes were left out due to insufficient knowledge of their optical properties from current literature data. The space occupied by these organs as well as any space between organs in the modified mouse torso was defined as adipose tissue.

All of the organs included in the modified phantom were assigned optical properties for wavelengths spanning the firefly luciferase emission spectrum (500–800 nm) reported by Kuo *et al*. The absorption (μ_a) and transport scattering (μ') coefficients assigned to each organ, as a function of photon wavelength (λ), were estimated on the basis of a compilation of relevant tissue optical property data reported in the literature (tables 1 and 2). An empirical function was employed to approximate $\mu'_s(\lambda)$:

$$\mu'_s(\lambda) = a \times \lambda^{-b}\,\mathrm{mm}^{-1}, \quad \lambda \text{ in nm} \tag{1}$$

where *a* and *b* were constants controlling the spectral variation in each tissue (table 1).

The amount of light absorption taking place in all tissues was assumed to depend only on the resident oxy-haemoglobin (HbO_2), deoxy-haemoglobin (Hb) and water (W) concentrations. The spectral absorption coefficient ($\mu_a(\lambda)$) was then approximated as a weighted sum of the three constituent absorption coefficients ($\mu_{aHbO_s}(\lambda)$, $\mu_{aHb}(\lambda)$ and $\mu_{aW}(\lambda)$), which were calculated from the corresponding absorbance spectra reported by Prahl (2001):

$$\mu_a(\lambda) = S_B(x\mu_{aHb}(\lambda) + (1 - x)\mu_{aHbO_2}(\lambda)) + S_W\mu_{aW}(\lambda) \tag{2}$$

where $x = (HbO_2)/((HbO_2)+(Hb))$ and S_B and S_W were heuristic scaling factors adjusted to match the absorption data currently available in the literature for each tissue (table 2). S_B and S_W were consistent with the known blood and water volume fractions respectively in the different mouse organs (Brown *et al* 1997) with the exception of the kidneys and the lungs. The blood volume fractions in these two organs predicted higher $\mu_a(\lambda)$ values than those reported in the literature.

It is important to emphasize that the tissue optical property literature data are sparse and incomplete. The publications compiled in table 1 report on measurements performed on tissues from different species, *in vitro* or *in vivo*, and at a great variety of other experimental conditions. In addition, the optical properties of the mouse stomach and bowel contents were unknown and this material could possibly shift around and mix with air pockets during image acquisition. In this work, the stomach and bowel contents were assumed to be homogeneous and static. They were assigned the abdomen optical properties as inferred from bulk tissue measurements (Torricelli *et al* 2001). Given the above shortcomings, it should be stated that the parametric descriptions that we assumed for equations (1) and (2) could only be interpreted as reasonable but rough estimates of the true mouse tissue optical properties.

The propagation of bioluminescence photons in the mouse torso phantom was first simulated by Monte Carlo (MC) methods. An open source MC code, originally intended for computing the time-resolved reflectance from photon sources located on the surface of optically heterogeneous media (Boas *et al* 2002), was modified to simulate the migration of photons emanating from sources at the mouse torso interior. The modified MC code required as inputs the discretized bioluminescence emission spectra, the voxelized distributed photon sources and the mouse torso optical property phantom. Although the background optical properties were a continuous function of photon wavelength, we have approximated the firefly luciferase emission spectrum (Kuo *et al* 2004) as five discrete intensity bins of 25 nm width each, centred

at 600, 625, 650, 675 and 700 nm respectively. Photons emitted at longer wavelengths comprised <1% of the total emission intensity and were ignored. Though photons from the firefly luciferase spectrum could be emitted at wavelengths as low as 500 nm, we found that these underwent extreme attenuation in all tissues and were therefore not included in the simulations. The mouse torso optical property phantom was defined as a cylindrical volume of 2 mm side cubic voxels. This rather coarse voxel size was employed in order to reduce memory and computation time requirements. Though the phantom's interior was voxelized, its air–tissue boundary was modelled as a smooth cylindrical surface. This was done to ensure that photons were refracting out of the phantom at the appropriate surface geometry, free of voxelation artefacts. Photons were subsequently scored at virtual detectors, of 2 mm × 2 mm size, which were located on the phantom's surface.

As MC simulations were time consuming (15 minutes on a 1.6 GHz PC for 10^6 photon histories) and their estimates for the photon flux reaching the phantom's surface inevitably contained statistical noise, we explored the alternative of using a deterministic code to perform these calculations. The publicly available time-resolved optical absorption and scattering tomography (TOAST) finite-element code (Arridge *et al* 1993, Schweiger *et al* 1995), which solves the diffusion approximation to the radiative transfer equation, was employed to compute the boundary fluxes resulting from point sources located in the mouse torso interior. The same optical property mouse phantom was used to match the MC simulation conditions. Though not used in this work, a smaller voxel size or even a non-segmented image volume of continuously varying optical properties could have been used to assign optical properties to the finite-element nodes defined in the TOAST code. A mesh generation tool which was part of the TOAST package was employed to discretize the mouse torso volume into tetrahedrons of an average 0.65 mm side size. This was sufficiently small to confer numerical stability to the diffusion computations. By comparing TOAST predictions with corresponding MC simulations we verified that, with the exception of sources located at <1 mm from the torso surface, the diffusion approximation was adequate. Figure 3 demonstrates the agreement between MC and TOAST in the case of a point source in the mouse gut, located 3 mm from the torso surface and emitting photons at 650 nm, for detector locations on the same transverse plane as the source. Similar results were found for all other bioluminescence emission wavelengths, source and detector locations considered in this work. However, in contrast to the MC code, TOAST could not handle non-scattering regions located within the geometric tissue boundaries. This presented a problem for modelling photon transport through the bladder. We verified by MC simulation that, for the detector field-of-view (FOV) locations examined in this work, the photon fluxes detected from point sources located at the edge of the FOV, and nearest to the bladder, were independent of the bladder's presence. Given this observation, the volume occupied by the bladder was filled with a scattering medium, chosen to be adipose tissue.

TOAST was advantageous to use over MC because it could calculate boundary photon fluxes with similar accuracy but in addition, its computations were free of statistical noise and were completed faster by a factor of 7, or more, on the same computer. Therefore, the TOAST code was employed to compute the photon fluxes from emission sources, located in internal organs, reaching each of the boundary elements of the mouse torso surface. These computations were the first step in simulating the virtual OPET detector measurements. A controlled amount of Gaussian noise, having zero mean and variance amplitude equal to the square root of photons crossing each boundary element, was then added to the noiseless flux calculations. In addition, a wavelength-dependent autoluminescence background flux (Troy *et al* 2004) was added to each of those photon counts as spatially invariant Gaussian noise. It was a reasonable approximation to assume that the angular distribution of diffuse photons exiting the mouse torso was isotropic (Martelli *et al* 1999). The noise-added photon counts from each torso boundary element were then geometrically projected onto the virtual OPET detectors by use of appropriate solid angle factors (Gotoh and Yagi 1971, Wielopolski 1984). Finally a

wavelength independent detection efficiency and dark noise, estimated at 10% and 35 counts s^{-1} respectively (Prout *et al* 2004), were also modelled into the virtual OPET measurements. Source contributions from each of the five wavelength bins in which the firefly luciferase spectrum was discretized were weighed by the fractional spectrum area that they subtended. The intensity of source voxels was adjusted to achieve any desired overall signal-to-noise ratio (SNR) at the detectors.

In addition to performing virtual measurements with the OPET detectors (2.2 mm × 2.2 mm, 384 in total) high resolution detectors spanning OPET's geometrical FOV and having an area equal to that of boundary finite elements (HiResOPET, 0.68 mm × 0.65 mm, 1740 in total) were also utilized. These idealized HiResOPET virtual detectors were located on the mouse torso surface and had 100% detection efficiency. Thus the performance of OPET detectors could be compared to that of superior ones capable of higher spatial sampling and ideal detection efficiency.

Bioluminescent source distributions were reconstructed by use of an EM algorithm for emission tomography (Shepp and Vardi 1982). One of the required inputs for the EM code was the *P*-matrix—the collection of probabilities that a photon emitted from any source location in the image volume would reach any given detector. The *P*-matrix needs to be computed once for any particular choice of tissue optical properties and organ topologies. We employed TOAST to compute the *P*-matrix for point sources located at the centre of all 2 mm size voxels of the virtual mouse torso phantom for all five wavelengths approximating the luciferase emission spectrum. These were very time-consuming calculations that collectively took approximately 3 weeks to complete on a cluster of 27 CPUs (2 GHz, 4 GB RAM each) which were available at our institute. The EM algorithm utilized the *P*-matrix to reconstruct the most likely distributed source that generated the simulated measurement data. A weakness of the EM algorithm was that there was no official stopping criterion (Hebert and Leahy 1989) and the latter had to be determined empirically. For our virtual mouse torso phantom and the OPET detection geometry (Rannou *et al* 2004) we found that the reconstructed images did not change significantly after 2500 iterations. All of the images presented in this work were reconstructed with 5000 iterations, which were completed in approximately 1 h on a single CPU.

3. Results

The need for tomographic bioluminescence measurements was first demonstrated by simulating the OPET detector data for the case of a point source located at the mouse torso centre (figure 4(a)). Even for noise-free detection, there is no intuitive way to infer the true depth of the point source, or even that it is indeed a point source, by simply looking at the detector data image (figure 4(b)). It is even harder to infer any conclusions about the true localization of the source when its intensity is not much larger than the detected background noise (figure 4(c)). An additional difficulty is that tissue optical properties vary with photon wavelength. Thus both photon propagation and detection need to be considered in a spectrally-resolved fashion.

It was first investigated whether the proposed OPET system could attain tomographic images from simulated monochromatic detector measurements. In these test cases the tissue optical properties were assumed to be known and the simulated detector data were noise free. For a point source located at the mouse torso centre emitting at 650 nm (figure 4(a)) the reconstructed source was placed near the torso surface (figure 5(a)), which was clearly not its true location. The apparent near-surface reconstructed source placement was also observed for simulated sources located at different tissue depths emitting monochromatically at any wavelength in the firefly luciferase spectrum. An attempt to improve point source localization by employing the higher resolution virtual detectors (see the methods) was unsuccessful. In fact, the total photon

counts reaching each detector from the reconstructed source intensity distribution were always nearly identical to those reaching these same detectors from the true point source location. The similarity in detected intensity profiles from two different monochromatic emission source distributions demonstrated the ill-posed nature of the problem which has been previously reported (Kuo *et al* 2004).

The ability to reconstruct the true location of point emission sources by use of measurements at two wavelengths was then investigated. When noiseless detector data were simulated for the point source in figure 4(a), now emitting both at 600 nm and 650 nm, the EM reconstruction recovered its true location (figure 5(b)). Similarly, the true locations of point sources anywhere in the mouse torso could be recovered when detector data from any two of the five wavelengths used in this work (see the methods) were used in the reconstructions. Inclusion of noiseless detector data at additional wavelengths did not substantially improve the quality of reconstructed images. Furthermore, it was examined whether noisy detector data at two wavelengths would still be sufficient for the EM reconstructions to recover the true locations of point sources. The same point source as in figure 4(a) was simulated to have an emission intensity sufficient to produce a total of OPET detector counts which was three standard deviations above the sum of the overall autoluminescence background and detector dark noise. Measurements at any two wavelengths yielded reconstructed images of a diffuse source distribution which encompassed the true source location (e.g. figure 5(c)). Measurements at three wavelengths improved the point source localization (figure 5(d)). Incremental inclusion of additional measurements at up to five wavelengths (figure 5(e)) further improved reconstructions though ever less so. Similar results were found for most point source locations within the detectors' geometrical FOV. Exceptions to these observations were any sources located deep within highly attenuating tissues, e.g. at the liver centre. In the latter case and for physiologically relevant source intensities (Troy *et al* 2004), photon count contributions from wavelengths below 650 nm were lower than background noise.

The above simulations were performed under the assumption that the mouse optical properties were known exactly. This is difficult to achieve by prior non-invasive optical measurements even when additional anatomical information is provided by some other high resolution imaging modality (Barnett *et al* 2003). In addition, time-consuming *P*-matrix calculations would need to be repeated for every mouse, which is impractical. We have examined the possibility of assuming a uniform optical property background for the mouse torso while reconstructing the measurements obtained from the heterogeneous torso phantom. We found that assigning the volume average optical properties of the whole mouse torso to the homogeneous phantom did not describe photon transport well in all regions of the optically heterogeneous torso. The reason was that the volume average properties were close to those of liver, which were too attenuating to accurately describe the photon transport in less attenuating tissues such as the gut. We decided to examine more closely the favourable case of having the OPET geometrical FOV encompass the less heterogeneous middle part of the torso which mostly contained adipose tissue and the gut ($\mu_a(\lambda)$ and $\mu'_s(\lambda)$ volume averages shown in table 3). Noiseless detector data from three separate point source locations, all located on an axial plane which was centred in the OPET FOV, were reconstructed. In the radial direction one source was located at the cylinder's centre, one at half-radius and one at the edge voxel (figure 6(a)). The reconstruction of the source at the centre was poor (figure 6(b)). The reconstructed source distribution at half-radius (figure 6(c)) was slightly mis-positioned relative to the true point source location and was somewhat diffuse. The point source at the cylinder's edge (figure 6(d)) was reconstructed at its correct location. These findings demonstrated that assumption of a uniform optical property background was appropriate only when point sources were superficial.

The capacity of OPET measurements to tomographically resolve two neighbouring-point sources at different tissue depths and in different organs was then explored for the case where the mouse optical properties were known exactly. The arbitrary criterion for considering the two sources resolved was that in a line profile through the image a trough, dipping at >15% of the two peak amplitudes' mean, would exist between the two source peak intensities. First, it was examined whether two point sources separated by a distance of 2 voxels (or 4 mm) could be resolved. When two such sources of equal intensity were placed on either side of the mouse torso centre in either the gut or the liver, they could not be resolved in the reconstructed images (figure 7(a), SNR = 5). In addition, these sources could also not be resolved for unequal relative intensity ratios (data not shown). When those source pairs were moved on either side of the torso half-radius, they could still not be resolved if they were of equal intensities (figure 7(b)). However, they could be resolved in the liver if their relative intensities were in the vicinity of 2:1 (figure 7(b)) but did not exceed 3:1. Finally, the two sources were moved near the torso edge so that the one nearest to the surface was located at 1 mm depth. Even at these superficial tissue depths two equal intensity sources in the gut could not be resolved but they could be resolved in the liver (figure 7(c)). Nevertheless, these two sources could actually be resolved for unequal intensity ratios ranging from 2:1 to 5:1 in the gut and for up to 10:1 in the liver (data not shown). When the two sources were separated by a centre-to-centre distance of $\geqslant$3 voxels, or 6 mm, they were always resolved at all tissue locations if the true tissue optical properties were assumed to be known. For example, two equal intensity point sources located in the gut and the spleen respectively could be resolved under these circumstances (figure 7 (d)). However, when a uniform optical property background was assumed the two point sources were reconstructed as a single source located half-way between the two true source locations (figure 7(d)). In all of the above cases where the two equal intensity point sources were resolved they were typically not reconstructed at equal intensities though they were within a factor of 4 of each other.

Interestingly, image reconstruction artefacts in the form of additional 'phantom' emission sources appeared at mouse torso locations from where emitted photons had a small probability of reaching the OPET detectors. For example in the case of two point sources, separated by 4 mm, in the gut (figure 8(a)) a phantom source appeared at the edge of the FOV and near the liver centre (figure 8(b), SNR = 5). The artefact persisted even for noiseless detector data (figure 8(c)) though its intensity was much weaker. A similar image artefact was observed in the heart blood pool area when the OPET FOV was shifted to the upper half of the mouse torso (data not shown). As photons emitted from these artefactual sources were highly attenuated, they did not contribute significantly to the total detected signal. Interestingly, these artefacts disappeared and the two point sources were better localized when virtual measurements were performed by the more numerous HiResOPET detectors located on the torso surface (figure 8 (d), SNR = 5). Nevertheless, even with measurements performed by these higher resolution detectors the two equal intensity sources at the torso centre were neither resolved nor were they reconstructed at equal intensities.

Finally the capacity to reconstruct distributed emission sources from OPET detector data was investigated. In two test cases the segmented volumes occupied by the kidneys (encircled green voxels in figure 9(a)) and the gut (green–yellow voxels in figure 9(d)) were each defined as distributed sources. The same emission intensity was assigned to all source voxels with each one contributing an overall SNR $\geqslant$ 5 at the OPET detectors. When the true torso optical properties were utilized in the reconstructions, the true spatial extents of the distributed sources defined by the kidneys (figure 9(b)) and the gut (figure 9(e)) were both recovered. As found previously, assumption of a uniform optical property background resulted in artefacts. The reconstructed kidneys volumes were shifted relative to their true locations and an apparent exclusion of source emission activity, similar to that seen in figure 6(b), could also be observed (figure 9(c)). The problem of emission source exclusion from the torso centre was seen more

clearly when the gut was reconstructed while assuming a uniform optical property background (figure 9(f)).

4. Discussion and conclusions

Simulations were performed to assess the capacity of a proposed OPET system to perform tomographic bioluminescence imaging. Measurements at a single wavelength were found to be inadequate for achieving three-dimensional source localization. The latter was not even obtained when the idealized HiResOPET detectors were employed, even though these were located on the phantom surface. Therefore the need for spectrally resolved detection to achieve tomographic bioluminescence imaging was independent of the imaging system specifics. Though OPET measurements at two wavelengths did produce tomographic images, source localization improved when additional spectral measurements were included. With the exception of sources located on the skin surface, photons emitted at wavelengths <600 nm suffered extreme attenuation in all tissues. In addition sources located deep in highly attenuating tissues, such as the liver centre, did not have significant signal contributions to the detectors for wavelengths <650 nm. Therefore, image reconstructions for experimental data from these source locations are expected to suffer not only from fewer photon counts but also from having a smaller fraction of the firefly luciferase spectrum available for spectrally resolved measurements.

The capacity of the OPET system to resolve two neighbouring point sources was a function of their locations in different tissues and decreased with tissue depth. It was also observed that two neighbouring sources were better resolved in the liver than in the gut even though the former was a more absorbing tissue. It is hypothesized that this was a result of the higher spatial gradient of spectral attenuation in the more absorbing tissues which would favour depth resolution. When two equal intensity point sources were resolved, they were typically not reconstructed at equal intensities. In addition, the range of relative intensity ratios for which two point sources could be resolved was a function of their locations in tissues. The overall dynamic range for resolving two neighbouring sources separated by 2 voxels (4 mm) was rather limited, not exceeding 4:1, unless these were located within a few mm of the tissue surface. It should nevertheless be noted that the limits in resolving neighbouring sources will not have been fully explored until image reconstructions utilizing *P*-matrices of 1 mm voxel size, or less, are performed. Given that the computation of the 2 mm voxel *P*-matrices used in this work was time consuming, use of higher resolution *P*-matrices is presently impractical.

The spatial distribution of photon fluence reaching the tissue surface depends both on the tissue optical properties and the size and shape of the mouse organs in which bioluminescence sources are embedded. Exact knowledge of the tissue optical properties in every mouse being imaged may not be practical or even possible. In addition the optical property map in the mouse changes with breathing and food digestion. Even if that dynamic optical property map was known it would be impractical to compute a new *P*-matrix for every mouse. On the other hand, the attempted simplification of assuming a uniform optical property background was shown to be inadequate unless emission sources were superficial. The above findings imply that development of computationally efficient methods taking into account the differences between individual mouse optical properties would be the key to any practical implementation of bioluminescence tomography. In future work we plan to explore image artefacts arising from assigning inaccurate optical properties to tissues whose anatomical boundaries are obtained by an independent high resolution imaging modality.

The detector spatial resolution was shown to play an important role in the quality of the resulting reconstructed images. The OPET detector spatial resolution was restricted to 2.2 mm. The latter was equal to the centre-to-centre distance between neighbouring PET crystals (block of 8 × 8,

2 mm × 2 mm each, 0.2 mm inter-crystal gap) which were designed to match the physical size of the channels on a 64-channel photomultiplier tube. Unfortunately, bioluminescence detection at 2.2 mm resolution resulted in reconstructed image artefacts in areas of high photon attenuation in the mouse. These artifacts were eliminated when the OPET detectors were replaced by the HiResOPET ones, which were simulated to have a width of approximately 650 μm—a resolution easily achievable by CCD cameras. These considerations indicate some of the compromises one is faced with when designing a hybrid imaging modality system.

The proposed OPET system presents a unique opportunity to determine the relative bioluminescence and PET tracer detection sensitivities as a function of source depth in the mouse in a spatially co-registered setting. Optical photons undergo both strong and spatially variable attenuation as they travel through tissues. Based on calculations performed in this work, typical OPET detection probabilities per bioluminescence photon emitted are 0.15% for a point source located at the mouse torso centre in the gut and 0.01% for one at the liver centre. Near the torso surface, bioluminescence photon detection probabilities are about 2%. In contrast, annihilation gamma photons undergo little (~20%) attenuation as they travel through the mouse but they are also hard to stop even by high-density detector materials. As a result small animal PET systems have an absolute sensitivity of the order of 4% (Chatziioannou 2002). It is important to remember though that the detected emission intensities from both PET and bioluminescence sources are also the functions of their respective tracer kinetics *in vivo* as well as the underlying cell biology of each tracer. Future comparisons between simultaneous optical and PET images will enable exploring the detection sensitivity of bioluminescence tomography under the design constraints of a dual modality system.

Acknowledgements

We would like to thank Dr Richard Taschereau for providing us with the schematic shown in figure 1. We would also like to thank Dr Martin Schweiger and Jason Riley of University College, London, for their advice on the use of the TOAST code. We would like to acknowledge Dr Richard Leahy, Dr Felix Darvas, and Abhijit Chaudhari of the University of Southern California for fruitful discussions and advice on finite-element bioluminescence computations. Finally, we would like to thank Dr Michael Patterson of McMaster University, Canada, for his comments on the manuscript. This work was supported by the NIBIB R01-EB001458, NIH/NCI R25 CA098010:01 and DE-FC02-02ER63520 grants.

References

Arridge SR, Schweiger M, Hiraoka M, Delpy DT. A finite element approach for modeling photon transport in tissue. 1993;20:299–309.

Barnett AH, Culver JP, Sorensen AG, Dale A, Boas DA. Robust inference of baseline optical properties of the human head with three-dimensional segmentation from magnetic resonance imaging. Appl Opt 2003;42:3095–108. [PubMed: 12790461]

Beek JF, Blokland P, Posthumus P, Aalders M, Pickering JW, Sterenborg HJCM, vanGemert MJC. *In vitro* double-integrating-sphere optical properties of tissues between 630 and 1064 nm. Phys Med Biol 1997a;42:2255–61. [PubMed: 9394410]

Beek JF, vanStaveren HJ, Posthumus P, Sterenborg HJCM, vanGemert MJC. The optical properties of lung as a function of respiration. Phys Med Biol 1997b;42:2263–72. [PubMed: 9394411]

Boas DA, Culver JP, Stott JJ, Dunn AK. Three dimensional Monte Carlo code for photon migration through complex heterogeneous media including the adult human head. Opt Express 2002;10:159–70.

Brown RP, Delp MD, Lindstedt SL, Rhomberg LR, Beliles RP. Physiological parameter values for physiologically based pharmacokinetic models. Toxicol Ind Health 1997;13:407–84. [PubMed: 9249929]

Chatziioannou AF. Molecular imaging of small animals with dedicated PET tomographs. Eur J Nucl Med Mol Imaging 2002;29:98–114. [PubMed: 11807613]

Chaudhari A J, Darvas F, Cherry S R and Leahy R M 2005 Resolution studies in bioluminescence and fluorescence optical tomography using hyperspectral data acquisition Mol. Imaging Biol. (Orlando) vol 7 (New York: Springer) p 125

Cheong WF, Prahl SA, Welch AJ. A review of the optical-properties of biological tissues. IEEE J Quantum Elect 1990;26:2166–85.

Contag PR, Olomu IN, Stevenson DK, Contag CH. Bioluminescent indicators in living mammals. 1998;4:245–7.

Doornbos RMP, Lang R, Aalders MC, Cross FW, Sterenborg HJCM. The determination of *in vivo* human tissue optical properties and absolute chromophore concentrations using spatially resolved steady-state diffuse reflectance spectroscopy. Phys Med Biol 1999;44:967–81. [PubMed: 10232809]

Enejder AMK, Swartling J, Aruna P, Andersson-Engels S. Influence of cell shape and aggregate formation on the optical properties of flowing whole blood. Appl Opt 2003;42:1384–94. [PubMed: 12638895]

Firbank M, Hiraoka M, Essenpreis M, Delpy DT. Measurement of the optical-properties of the skull in the wavelength range 650–950 nm. Phys Med Biol 1993;38:503–10. [PubMed: 8488176]

Gotoh H, Yagi H. Solid angle subtended by a rectangular slit. Nucl Inst Methods 1971;96:485–6.

Hebert T, Leahy R. A generalized Em algorithm for 3-D Bayesian reconstruction from poisson data using Gibbs priors. IEEE Trans Med Imaging 1989;8:194–202.

Holboke MJ, Tromberg BJ, Li X, Shah N, Fishkin J, Kidney D, Butler J, Chance B, Yodh AG. Three-dimensional diffuse optical mammography with ultrasound localization in a human subject. J Biomed Opt 2000;5:237–47. [PubMed: 10938789]

Jacques SL, Prahl SA. Modeling optical and thermal distributions in tissue during laser irradiation. Laser Surg Med 1987;6:494–503.

Karagiannes JL, Zhang Z, Grossweiner B, Grossweiner LI. Applications of the 1-D diffusion-approximation to the optics of tissues and tissue phantoms. Appl Opt 1989;28:2311–7.

Kienle A, Lilge L, Patterson MS, Hibst R, Steiner R, Wilson BC. Spatially resolved absolute diffuse reflectance measurements for noninvasive determination of the optical scattering and absorption coefficients of biological tissue. Appl Opt 1996;35:2304–14.

Kuo C, Coquoz O, Stearns D G and Rice B 2004 Diffuse luminescence tomography of in vivo bioluminescent markers using multi-spectral data Society for Molecular Imaging 3rd Annual Meeting (St. Louis) vol 3 (Cambridge: MIT Press) p 227

Lualdi M, Colombo A, Farina B, Tomatis S, Marchesini R. A phantom with tissue-like optical properties in the visible and near infrared for use in photomedicine. Laser Surg Med 2001;28:237–43.

Marchesini R, Bertoni A, Andreola S, Melloni E, Sichirollo AE. Extinction and absorption-coefficients and scattering phase functions of human-tissues *in vitro*. Appl Opt 1989;28:2318–24.

Martelli F, Sassaroli A, Zaccanti G, Yamada Y. Properties of the light emerging from a diffusive medium: angular dependence and flux at the external boundary. Phys Med Biol 1999;44:1257–75. [PubMed: 10368017]

Matern U, Haberstroh J, el Saman A, Pauly E, Salm R, Farthmann EH. Emergency laparoscopy: technical support for the laparoscopic diagnosis of intestinal ischemia. Surg Endosc 1996;10:883–7. [PubMed: 8703143]

Mitic G, Kolzer J, Otto J, Plies E, Solkner G, Zinth W. Time-gated transillumination of biological tissues and tissuelike phantoms. Appl Opt 1994;33:6699–710.

Parsa P, Jacques SL, Nishioka NS. Optical-properties of rat-liver between 350 and 2200 nm. Appl Opt 1989;28:2325–30.

Pifferi A, Torricelli A, Taroni P, Bassi A, Chikoidze E, Giambattistelli E, Cubeddu R. Optical biopsy of bone tissue: a step toward the diagnosis of bone pathologies. J Biomed Opt 2004;9:474–80. [PubMed: 15189084]

Prahl S A 2001 http://omlc.ogi.edu/spectra/index.html Oregon Medical Laser Clinic

Prout DL, Silverman RW, Chatziioannou A. Detector concept for OPET—a combined PET and optical Imaging system. IEEE Trans Nucl Sci 2004;51:752–6. [PubMed: 16429601]

Rannou FR, Kohli V, Prout DL, Chatziioannou AF. Investigation of OPET performance using GATE, a Geant4-based simulation software. IEEE Trans Nucl Sci 2004;51:2713–7. [PubMed: 16429604]

Ray P, De A, Min JJ, Tsien RY, Gambhir SS. Imaging tri-fusion multimodality reporter gene expression in living subjects. Cancer Res 2004;64:1323–30. [PubMed: 14973078]

Ray P, Wu AM, Gambhir SS. Optical bioluminescence and positron emission tomography imaging of a novel fusion reporter gene in tumor xenografts of living mice. Cancer Res 2003;63:1160–5. [PubMed: 12649169]

Ritz JP, Roggan A, Germer CT, Isbert C, Muller G, Buhr HJ. Continuous changes in the optical properties of liver tissue during laser-induced interstitial thermotherapy. Laser Surg Med 2001;28:307–12.

Schweiger M, Arridge SR, Hiraoka M, Delpy DT. The finite-element method for the propagation of light in scattering media—boundary and source conditions. Med Phys 1995;22:1779–92. [PubMed: 8587533]

Segars WP, Tsui BM, Frey EC, Johnson GA, Berr SS. Development of a 4-D digital mouse phantom for molecular imaging research. Mol Imaging Biol 2004;6:149–59. [PubMed: 15193249]

Shepp LA, Vardi Y. Maximum likelihood reconstruction for emission tomography. IEEE Trans Med Imaging 1982;1:113–22.

Solonenko M, Cheung R, Busch TM, Kachur A, Griffin GM, Vulcan T, Zhu TC, Wang HW, Hahn SM, Yodh AG. *In vivo* reflectance measurement of optical properties, blood oxygenation and motexafin lutetium uptake in canine large bowels, kidneys and prostates. Phys Med Biol 2002;47:857–73. [PubMed: 11936174]

Srinivasan S, Pogue BW, Jiang SD, Dehghani H, Kogel C, Soho S, Gibson JJ, Tosteson TD, Poplack SP, Paulsen KD. Interpreting hemoglobin and water concentration, oxygen saturation, and scattering measured *in vivo* by near-infrared breast tomography. Proc Natl Acad Sci USA 2003;100:12349–54. [PubMed: 14514888]

Swartling J, Palsson S, Platonov P, Olsson SB, Andersson-Engels S. Changes in tissue optical properties due to radio-frequency ablation of myocardium. Med Biol Eng Comput 2003;41:403–9. [PubMed: 12892362]

Tai C, Chatziioannou A, Siegel S, Young J, Newport D, Goble RN, Nutt RE, Cherry SR. Performance evaluation of the microPET P4: a PET system dedicated to animal imaging. Phys Med Biol 2001;46:1845–62. [PubMed: 11474929]

Thueler P, Charvet I, Bevilacqua F, St Ghislain M, Ory G, Marquet P, Meda P, Vermeulen B, Depeursinge C. *In vivo* endoscopic tissue diagnostics based on spectroscopic absorption, scattering, and phase function properties. J Biomed Opt 2003;8:495–503. [PubMed: 12880356]

Torricelli A, Pifferi A, Taroni P, Giambattistelli E, Cubeddu R. *In vivo* optical characterization of human tissues from 610 to 1010 nm by time-resolved reflectance spectroscopy. Phys Med Biol 2001;46:2227–37. [PubMed: 11512621]

Torricelli A, Quaresima V, Pifferi A, Biscotti G, Spinelli L, Taroni P, Ferrari M, Cubeddu R. Mapping of calf muscle oxygenation and haemoglobin content during dynamic plantar flexion exercise by multi-channel time-resolved near-infrared spectroscopy. Phys Med Biol 2004;49:685–99. [PubMed: 15070196]

Troy T, Jekic-McMullen D, Sambucetti L, Rice B. Quantitative comparison of the sensitivity of detection of fluorescent and bioluminescent reporters in animal models. Mol Imaging 2004;3:9–23. [PubMed: 15142408]

Ugryumova N, Matcher SJ, Attenburrow DP. Measurement of bone mineral density via light scattering. Phys Med Biol 2004;49:469–83. [PubMed: 15012014]

Wang G, Li Y, Jiang M. Uniqueness theorems in bioluminescence tomography. Med Phys 2004;31:2289–99. [PubMed: 15377096]

Wei HJ, Xing D, Wu GY, Jin Y, Gu HM. Optical properties of human normal small intestine tissue determined by Kubelka–Munk method *in vitro*. World J Gastroentero 2003;9:2068–72.

Wielopolski L. Monte Carlo calculation of the average solid angle subtended by a parallellepiped detector from a distributed source. Nucl Instum Methods Phys Res 1984;226:436–48.

Zijp JR, ten Bosch JJ. Optical properties of bovine muscle tissue *in vitro*: a comparison of methods. Phys Med Biol 1998;43:3065–81. [PubMed: 9814535]

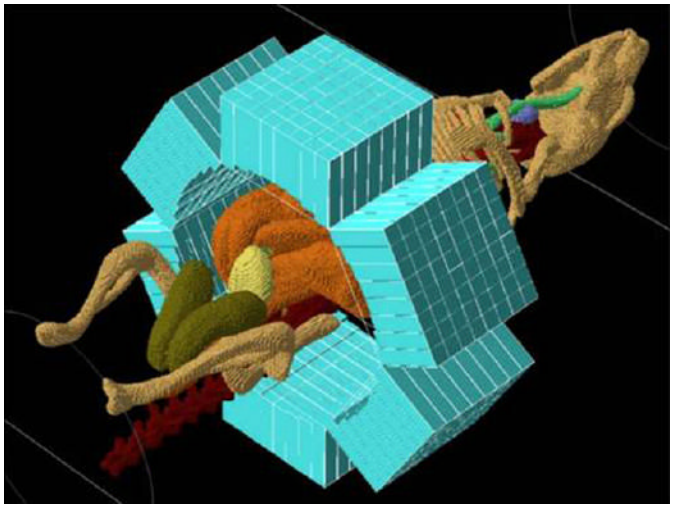

Figure 1.
A schematic of the proposed OPET system. Its gantry size is only slightly larger than the mouse torso diameter.

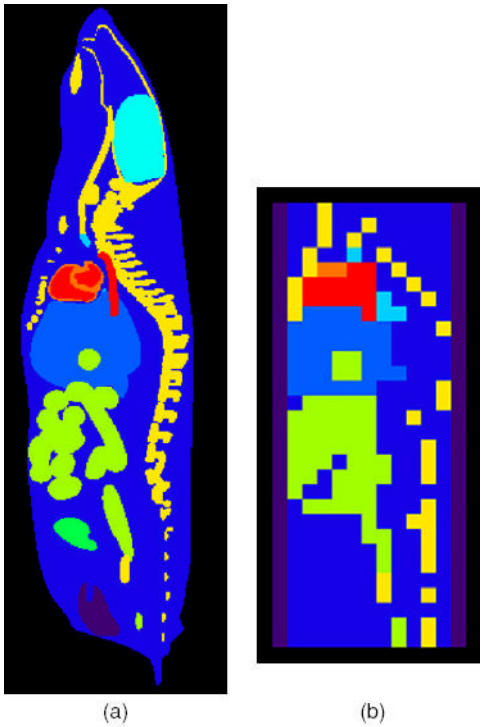

Figure 2.
(a) Sagittal view of the MOBY mouse. (b) Corresponding sagittal view for the modified mouse torso phantom. Different colours correspond to different tissue types (dark blue: adipose tissue, light blue: liver, turquoise: lungs, yellow: bone, red: whole blood, orange: heart wall, light green: gut, and purple: skin).

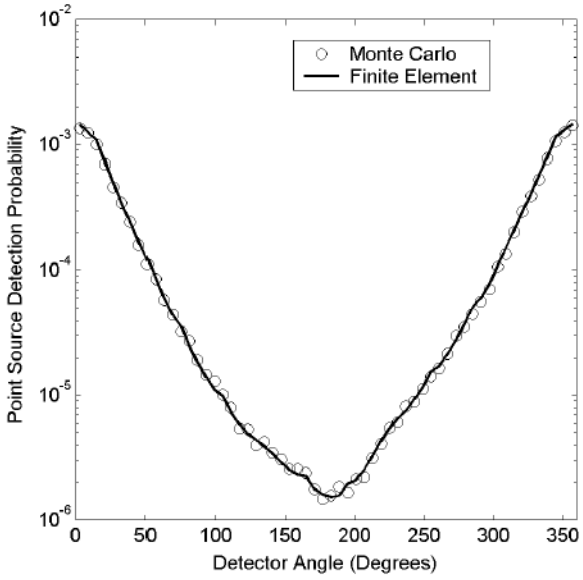

Figure 3.
Comparison between MC and TOAST boundary flux predictions for a 3 mm deep point source in the mouse gut emitting at 650 nm. Results are shown for a single ring of HiResOPET detectors centred on the axial plane containing the point source.

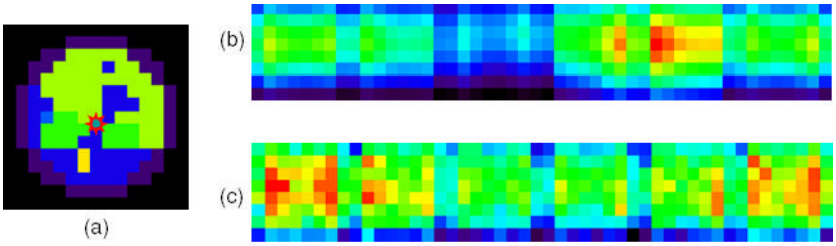

Figure 4.
(a) Transverse view of the mouse torso gut area with a point source located at its centre (star). (b) Noise-free and spectrally blind OPET detector measurements for the point source described in (a), emitting at wavelengths and spectral intensities defined by the luciferase spectrum. (c) As in (b) but with the point source emitting at an intensity that is three times higher than the standard deviation of background noise as measured at the mouse torso surface. The six OPET detector blocks can be discerned.

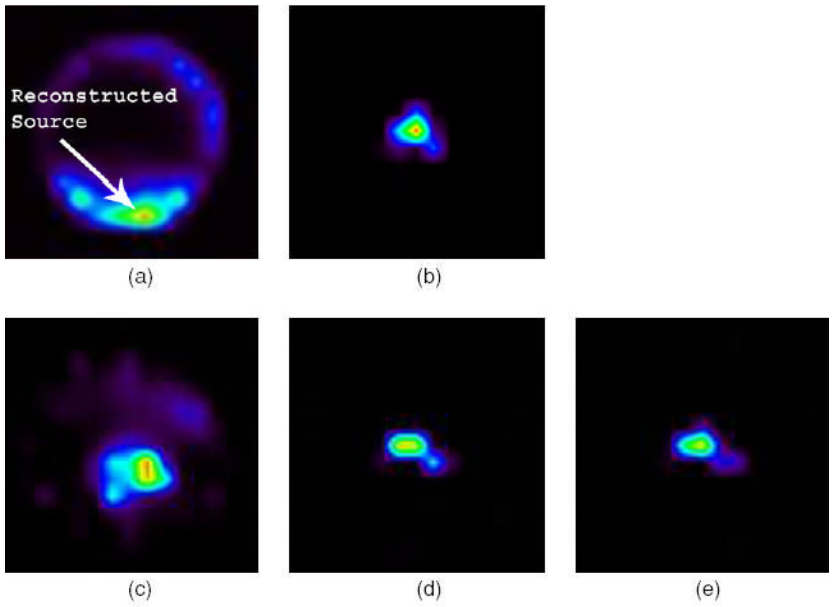

Figure 5.

(a) Reconstructed source distribution based on noiseless boundary flux data generated by the point source in figure 4(a) emitting at 650 nm. (b) As in (a) but for spectrally distinct detection of photons emitted simultaneously at 625 nm and 650 nm. (c) Reconstructed source distribution for spectrally distinct detection of noise-added boundary flux data generated by the point source in figure 4(a) emitting at 625 nm and 650 nm. (d) As in (c) but with the source emitting at 600, 625 and 650 nm. (e) As in (c) but with the source emitting at 600, 625, 650, 675 and 700 nm.

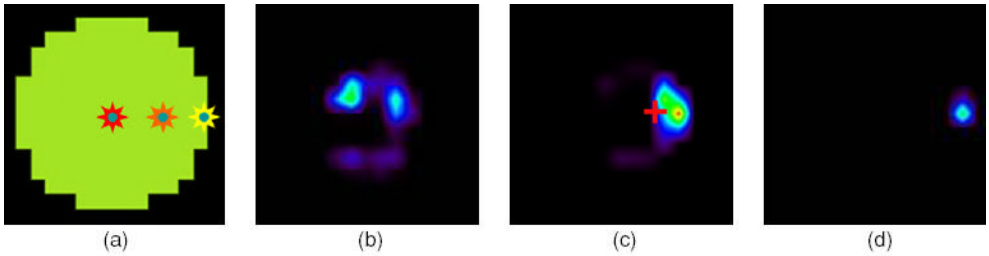

Figure 6.

(a) Transverse view of the homogeneous mouse torso with three individually simulated point sources sequentially placed at its centre, at half-radius and at 1 mm from the surface. (b) Reconstructed source distribution based on noiseless boundary flux data generated by the point source at the torso centre emitting at all five wavelengths. (c) As in (a) but for a source located at half-radius; the red cross indicates the correct position of the point source. (d) As in (a) but for a source located at 1 mm from the surface.

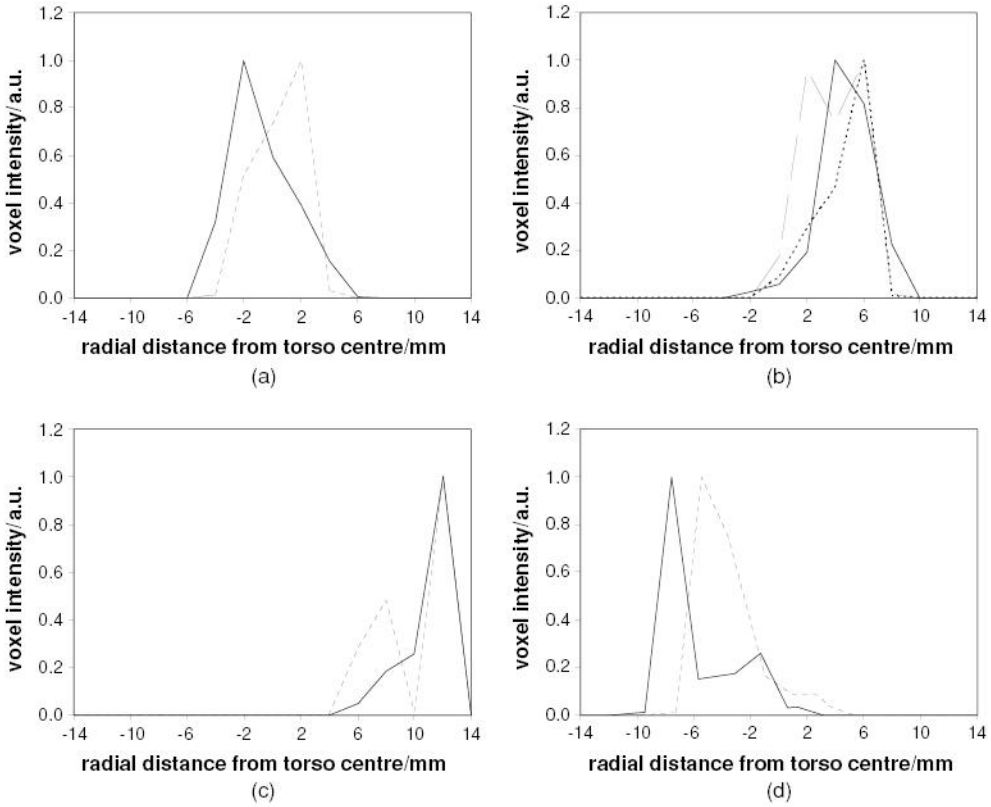

Figure 7.

Line profiles through the two source peak intensities in reconstructed images of source pairs in different anatomical locations. (a) Equal intensity sources separated by 4 mm in the gut (solid curve) and the liver (short dashed curve). (b) As in (a) but with the two sources located symmetrically around the torso half-radius. The two sources could be resolved in the liver for a relative intensity ratio of 2:1 (grey long dashed curve). (c) As in (a) but with the two sources located at 1 mm and 5 mm from the torso surface. (d) Two equal intensity point sources, 6.3 mm apart, when the true tissue optical properties (solid curve) and a uniform optical property background (short dashed curve) were utilized in the image reconstructions.

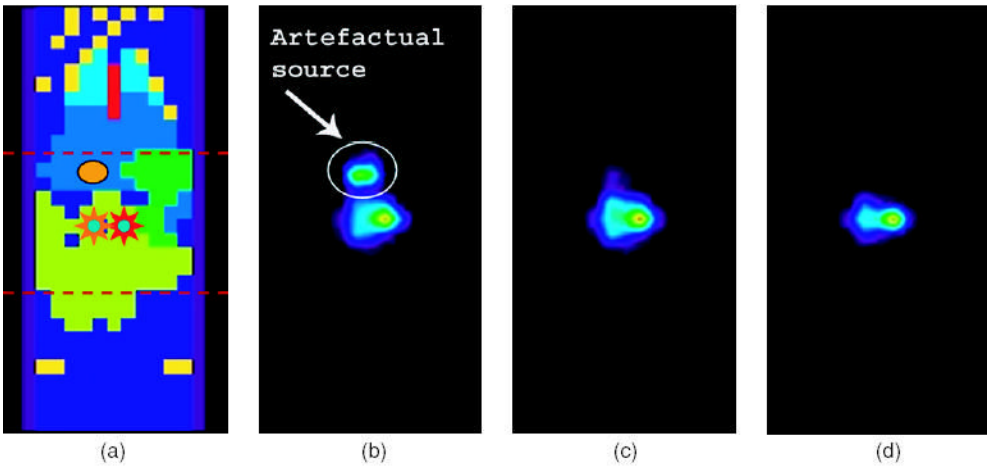

Figure 8.
(a) Coronal view of the mouse torso phantom with two equal intensity point sources (red stars) located on either side of the torso centre in the gut. The artefactual source (orange oval) was located at the liver centre and near the OPET FOV (red dashed lines) edge. (b) Reconstructed image of the two point sources based on the OPET detector measurements at SNR = 5. (c) As in (b) but for noiseless detector data. (d) Reconstructed image based on the virtual HiResOPET detector measurements at SNR = 5.

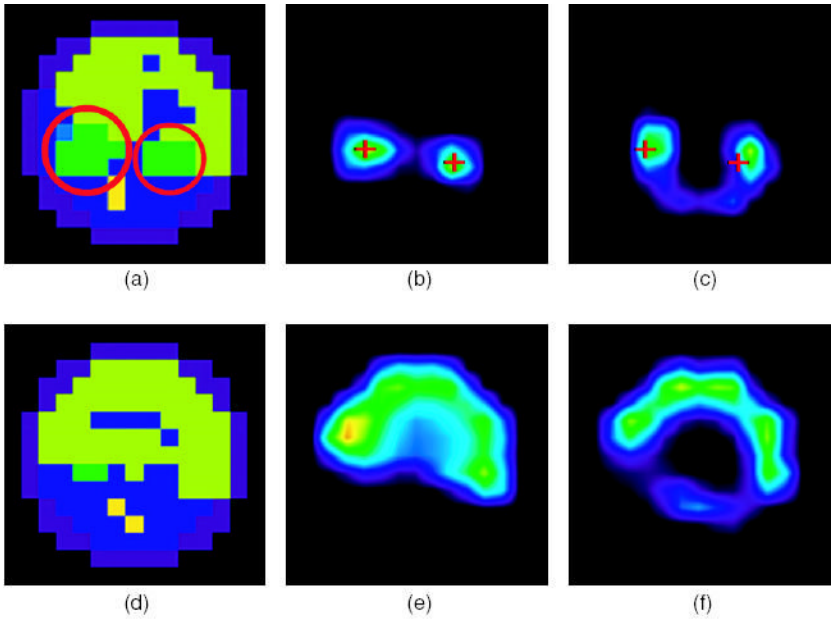

Figure 9.

(a) Transverse view of the mouse torso for an axial slice through the kidneys (encircled green voxels). (b) Transverse view of the kidneys reconstructed as a uniform distributed source. The red crosses indicate the peak intensity value in each kidney. (c) As in (b) but assuming a uniform optical property background. The red crosses indicate a shift in the reconstructed kidney source locations. (d) Transverse view of the mouse torso for an axial slice through the gut (yellow–green voxels). (e) Transverse view of the gut reconstructed as a uniform distributed source. (f) As in (e) but assuming a uniform optical property background.

Table 1

Values for the parameters *a* and *b* used to estimate $\mu'_s(\lambda)$ for each tissue by use of equation (1). Definitions of these parameters are provided in the text.

Tissue type	*a* (mm^{-1})	*b* (no units)	References
Adipose	38.0	0.53	(Mitic *et al* 1994, Kienle *et al* 1996, Holboke *et al* 2000, Srinivasan *et al* 2003)
Bone	35600	1.47	(Firbank *et al* 1993, Beek *et al* 1997a, 1997b, Pifferi *et al* 2004, Ugryumova *et al* 2004)
Bowel	3670	1.24	(Matern *et al* 1996, Torricelli *et al* 2001, Solonenko *et al* 2002, Wei *et al* 2003)
Heart wall	10600	1.43	(Swartling *et al* 2003)
Kidneys	41700	1.51	(Solonenko *et al* 2002)
Liver and spleen	629	1.05	(Karagiannes *et al* 1989, Marchesini *et al* 1989, Parsa *et al* 1989, Kienle *et al* 1996, Beek *et al* 1997a, 1997b, Ritz *et al* 2001, Srinivasan *et al* 2003)
Lung	68.4	0.53	(Beek *et al* 1997a, Beek *et al* 1997b, Srinivasan *et al* 2003)
Muscle	4.e7	2.82	(Cheong *et al* 1990, Kienle *et al* 1996, Beek *et al* 1997a, 1997b, Zijp and ten Bosch 1998, Torricelli *et al* 2004)
Skin	2850	1.1	(Jacques and Prahl 1987, Marchesini *et al* 1989, Beek *et al* 1997a, 1997b, Doornbos *et al* 1999, Lualdi *et al* 2001)
Stomach wall	792	0.97	(Thueler *et al* 2003)
Whole blood	133	0.66	(Enejder *et al* 2003)

Table 2

Values for the parameters *S*, *x*, and *y* used to estimate $\mu_a(\lambda)$ for each tissue by use of equation (2). Definitions of these parameters are provided in the text. The literature references employed for these estimates are identical to those in table 1.

Tissue type	S_B	x	S_W
Adipose	0.0033	0.7	0.5
Bone	0.049	0.8	0.15
Bowel	0.0093	0.8	0.5
Heart wall	0.05	0.75	0.5
Kidneys	0.056	0.75	0.8
Liver and spleen	0.30	0.75	0.7
Lung	0.15	0.85	0.85
Muscle	0.07	0.8	0.5
Skin	0.06	0.75	0.5
Stomach wall	0.01	0.7	0.8
Whole blood	1.0	0.75	0.0

Table 3

The uniform mouse torso optical property values at the five wavelengths used in this work.

Emission wavelength	$\mu_a(\lambda)$ (mm^{-1})	$\mu'_s(\lambda)$ (mm^{-1})
600	0.19	1.66
625	0.062	1.59
650	0.038	1.53
675	0.028	1.47
700	0.022	1.41